

# Synthesis and Photoluminescence Properties of Rare-Earth-Activated $\text{Sr}_{3-x}\text{A}_x\text{AlO}_4\text{H}$ ( $\text{A} = \text{Ca}, \text{Ba}; x = 0, 1$ ): New Members of Aluminate Oxyhydrides

Tong Wu, Kotaro Fujii, Taito Murakami, Masatomo Yashima, and Satoru Matsuishi\*



Cite This: <https://dx.doi.org/10.1021/acs.inorgchem.0c02356>



Read Online

ACCESS |



Metrics & More

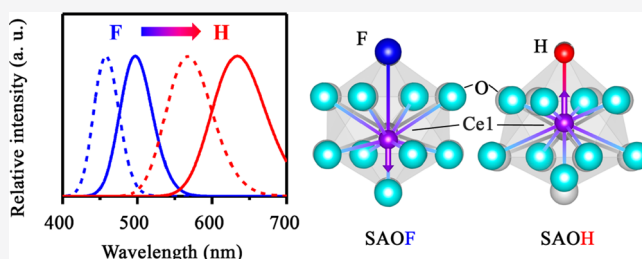


Article Recommendations



Supporting Information

**ABSTRACT:** A series of aluminate-based oxyhydrides,  $\text{Sr}_{3-x}\text{A}_x\text{AlO}_4\text{H}$  ( $\text{A} = \text{Ca}, \text{Ba}; x = 0, 1$ ), has been synthesized by high-temperature reaction of oxide and hydride precursors under a  $\text{H}_2$  atmosphere. Their crystal structures determined via X-ray and neutron powder diffraction are isostructural with tetragonal  $\text{Sr}_3\text{AlO}_4\text{F}$  (space group  $I4/mcm$ ), consisting of  $(\text{Sr}_{1-x/3}\text{A}_{x/3})_2\text{H}$  layers and isolated  $\text{AlO}_4$  tetrahedra. Rietveld refinement based on the diffraction patterns and bond-valence-sum analysis show that Ba preferentially occupies the 10-coordinated Sr1 sites, while Ca strongly prefers to occupy the 8-coordinated Sr2 sites. Luminescence owing to the  $4f-5d$  transition of  $\text{Eu}^{2+}$  or  $\text{Ce}^{3+}$  was observed from Eu- and Ce-doped samples,  $\text{Sr}_{3-x-y}\text{A}_x\text{B}_y\text{AlO}_4\text{H}$  ( $\text{A} = \text{Ca}, \text{Ba}; \text{B} = \text{Eu}, \text{Ce}; x = 0, 1, y = 0.02$ ), under excitation of near-ultraviolet light. Compared with its fluoride analogue,  $\text{Sr}_3\text{AlO}_4\text{H}:\text{Ce}^{3+}$  shows red shifts of both the excitation and emission bands, which is consistent with the reported hydride-based phosphors and can be explained by the covalency of the hydride ligands. The observed luminescence spectra can be decomposed into two sets of sub-bands corresponding to  $\text{Ce}^{3+}$  centers occupying Sr1 and Sr2 sites with distinctly different Stokes shifts (1.27 and 0.54 eV, respectively), as suggested by the results of constrained density functional theory (cDFT). The cDFT results also suggest that the large shift for  $\text{Ce}^{3+}$  at Sr1 is induced by large distortion of the coordinated structure with shortening of the H–Ce bond in the excited state. The current findings expand the class of oxyhydride materials and show the potential of hydride-based phosphors for optical applications.



## INTRODUCTION

Advances in solid-state materials, the exploration of mixed-anion compounds with more than one anionic substance in a single phase, have attracted enormous interest.<sup>1</sup> To obtain desirable functions, partial replacement of the oxide ligands in the coordinated sphere by different anions can effectively alter classical oxides. This includes tuning of the crystal-field splitting (CFS), modification of the valence-band maximum to adjust the electronic structure, tuning of the bonding nature between covalency and ionicity, and reduction of the dimensionality.<sup>2–5</sup> In addition, owing to the unique characteristics of anions, the incorporation of different anions is expected to offer a new pathway for materials design with distinctive chemical and physical properties.

Hydride ( $\text{H}^-$ ) and fluoride ( $\text{F}^-$ ) ions have similar ionic radii with the same charge, which provides the possibility of analogous structures in mixed-anion systems.<sup>6,7</sup> The  $\text{H}^-$  ion has some unique features because of the large polarizability ascribed to its electronic structure consisting of one proton with two electrons and the smaller electronegativity of H (2.20 in the Pauling scale) than that of F (3.98).<sup>8,9</sup> These differences can be sharply distinguished and strongly affect their chemical bonding nature. Therefore, mutual substitution of anion sites

suggests a new strategy to design novel functional oxyfluoride and oxyhydride compounds, and a comparison between them is essential for a thorough understanding of the effects of the hydride ligands.

As the most promising solid-state lighting source, phosphor-converted white-light-emitting diodes (pc-WLEDs) have been in focus for many years. They have many advantages over conventional lighting technologies, including remarkable luminous efficacy, long lifetime, high color quality, and low energy consumption.<sup>10</sup> The most commercially used pc-LEDs are based on blue or violet LED chips with the combination of multiphased phosphors to produce uniform white light.<sup>11</sup> To obtain phosphors with diverse luminescence properties, a number of different classes of compounds have been investigated, such as oxides, halides, oxyhalides, nitrides, and

Received: August 7, 2020

oxyhydrides doped with rare-earth metal ions (e.g., Ce<sup>3+</sup> and Eu<sup>2+</sup>).<sup>12–17</sup>

In addition to conventional host materials, rare-earth-activated hydride-based compounds possessing large red shifts in both the excitation and emission bands owing to the strong nephelauxetic effect (covalency) of H are expected to be new wavelength conversion materials.<sup>18–20</sup> However, most hydrides are so sensitive to the moisture in air that they have not been well investigated as practical materials. Recently, some oxyhydrides have been demonstrated to be phosphor hosts with moisture resistance while providing emission characteristics unique to hydride ligands.<sup>21–23</sup> In particular, Sr<sub>2</sub>LiSiO<sub>4</sub>H:Eu<sup>2+</sup>, which is isostructural to the silicate fluoride green phosphor Sr<sub>2</sub>LiSiO<sub>4</sub>F:Eu<sup>2+</sup>, shows intense yellow luminescence by near-ultraviolet (UV) excitation, indicating the possibility of novel oxyhydride phosphors derived from F-containing silicate and related minerals.

In this Article, we report the new oxyhydride system Sr<sub>3–x</sub>A<sub>x</sub>AlO<sub>4</sub>H (A = Ca, Ba; x = 0, 1) synthesized by solid-state reactions and its phosphor host properties. The synthesized samples can be handled in air for 1–10 days, unlike the previously reported aluminate-based oxyhydride Ba<sub>3</sub>AlO<sub>4</sub>H (orthorhombic, *Pnma*), which is extremely sensitive to air and moisture.<sup>24,25</sup> Rietveld analysis of the neutron powder diffraction (NPD) patterns of the D-enriched samples shows that the crystalline phases are isostructural to Sr<sub>3</sub>AlO<sub>4</sub>F (also denoted as SAOF; tetragonal, *I4/mcm*) with full occupation of D ions on the F sites. Isovalent substitution of Ba<sup>2+</sup> and Ca<sup>2+</sup> in Sr<sub>3</sub>AlO<sub>4</sub>H (also denoted as SAOH) shows the opposite site preference, and both can improve the overall stability. The Eu-doped Sr<sub>3–x</sub>A<sub>x</sub>AlO<sub>4</sub>H (A = Ca, Ba; x = 0, 1) compounds emit green luminescence with a narrow emission band centered at 510–530 nm. In place of Eu<sup>2+</sup> used for hydride and oxyhydride hosts in previous studies, we also applied Ce<sup>3+</sup> ions as activators with shorter luminescence lifetimes and higher radiative transition probabilities than those of Eu<sup>2+</sup>, which are ideal properties for high-power LED application.<sup>26–29</sup> The Ce-doped Sr<sub>3–x</sub>A<sub>x</sub>AlO<sub>4</sub>H (A = Ca, Ba; x = 0, 1) compounds reveal a broad emission band centered at 510 nm under excitation of near-UV light, which makes them suitable as phosphors for WLEDs. In particular, the luminescence center of Ce<sup>3+</sup> and the luminescence properties of SAOH are discussed by both experimental and theoretical analyses.

## EXPERIMENTAL SECTION

The polycrystalline Sr<sub>3–x</sub>A<sub>x</sub>AlO<sub>4</sub>H (A = Ca, Ba; x = 0, 1) samples were prepared by a solid-state reaction of oxides and hydrides at high temperature: 5SrO + (1 – 2x)SrH<sub>2</sub> + 2xAH<sub>2</sub> + Al<sub>2</sub>O<sub>3</sub> → 2Sr<sub>3–x</sub>A<sub>x</sub>AlO<sub>4</sub>H. SrO (99.9%), BaO (99%), and Al<sub>2</sub>O<sub>3</sub> were purchased from Sigma-Aldrich, Kojundo Chemical Laboratory, and Wako, respectively. CaO was obtained by calcining CaCO<sub>3</sub> (99.99%, Kojundo) at 1300 °C for 10 h in air and quenching to room temperature in a vacuum environment. The metal hydrides SrH<sub>2</sub>, CaH<sub>2</sub>, BaH<sub>2</sub>, EuH<sub>2</sub>, and CeH<sub>2</sub> were obtained by heating the metals at 400 °C under 0.99 MPa H<sub>2</sub> for 10 h. Because hydrides are sensitive to ambient air and moisture, the following experiments were conducted in an Ar-filled glovebox. Stoichiometric amounts of the starting compounds were intimately mixed in an alumina mortar and pressed into a pellet (diameter 6 mm). The pellet was covered by iron foil, placed in a stainless tube, and sintered at 900 °C for 12 h in a 0.99 MPa H<sub>2</sub> atmosphere. The resulting products were ground and stored in the glovebox for the following measurements.

The powder X-ray diffraction (XRD) patterns were collected at room temperature by a D8 Advance diffractometer with Cu K $\alpha$  radiation (Bruker, Germany), and analysis was performed by the

Rietveld method using the TOPAS code.<sup>30</sup> The air and moisture stability of the oxyhydride materials was determined by checking the XRD patterns at intervals after the samples were exposed to ambient air.

The density functional theory (DFT) calculations were performed by using the Vienna ab initio simulation package (VASP) code with the projector-augmented-wave method and Perdew–Burke–Ernzerhof (PBE) functional for generation of the band structure and projected density of states (PDOS) plots of SAOH.<sup>31–33</sup> The hybrid functional with Heyd–Scuseria–Ernzerhof (HSE06) was carried out to estimate the band-gap energies with a 2 × 2 × 2 *k*-point mesh and a cutoff energy of 600 eV.

Time-of-flight neutron powder diffraction (TOF-NPD) of the D-enriched sample (Sr<sub>3</sub>AlO<sub>4</sub>D, SAOD) was measured with an iMATERIA neutron diffractometer installed at beamline BL20 of the Material and Life Science Facility at the Japan Proton Accelerator Research Complex (J-PARC).<sup>34</sup> Cylindrical absorption corrections were applied to the TOF-NPD data using the inner diameter of the sample holder (5.8 mm) and the measured density (1.405 g cm<sup>–3</sup>). Rietveld refinement was carried out with the Z-code computer program for the TOF-NPD data taken with 90° bank (time focusing point at 2 $\theta$  = 90°).<sup>34</sup>

The H content of SAOH was estimated by thermal desorption spectroscopy (TDS) measurements using a TDS1400TV spectrometer (ESCO, Japan). The measurements were performed under a vacuum environment (below 10<sup>–7</sup> Pa), and the sample was heated from room temperature to 1473 K at a ramping rate of 60 K min<sup>–1</sup>. The diffuse-reflectance spectrometry (DRS) spectra were collected for polycrystalline samples over the spectral range of 200–1000 nm in an integrating sphere with MgO as the reflection standard by a Hitachi U4100 spectrophotometer in an ambient atmosphere. The Fourier transform infrared (FTIR) DRS spectra were taken with a Frontier spectrometer (PerkinElmer, Inc., USA) in air at room temperature with alumina-coated SiC abrasive pads as the reference. The valence state of Eu in SAOH:Eu was determined by magnetization measurements using a SQUID vibrating-sample magnetometer (Quantum Design MPMS). The magnetization (*M*) versus magnetic field (*H*) plots were obtained from –7 to +7 T under the fixed temperature *T* = 2.5 K. The *M* versus temperature (*T*) plots were obtained from 2.5 to 300 K with the fixed magnetic field *H* = 1 T. Both the *M*–*H* and *M*–*T* curves are fitted by the equation

$$M = N g \mu_B B_J(x)$$

where *N* is the number of atoms, *B<sub>J</sub>*(*x*) is the Brillouin function

$$B_J(x) = \frac{2J+1}{2J} \coth\left(\frac{2J+1}{2J}x\right) - \frac{1}{2J} \coth\left(\frac{1}{2J}x\right)$$

and *x* is given by  $x = g\mu_B/k_B T$  with the total angular momentum *J*, Landé factor *g* = 2, Bohr magneton  $\mu_B = 9.274 \times 10^{-21}$ , and Boltzmann constant  $k_B = 1.38065 \times 10^{-16}$ . Here, we chose *J* = 7/2, which corresponds to Eu<sup>2+</sup> with the <sup>8</sup>S<sub>7/2</sub> state. The photoluminescence excitation (PLE) and emission (PL) spectra of Sr<sub>3–x</sub>A<sub>x</sub>AlO<sub>4</sub>H:Ce<sup>3+</sup> were measured at room temperature by an F-4500 fluorescence spectrophotometer (Hitachi High-Technologies, Japan). To evaluate the emission lifetime, time decay curves were measured by using the third harmonic of the Nd:YAG laser ( $\lambda$  = 355 nm) with a pulse width of 7 ns as an excitation source and a fast-gated intensified charge-coupled-device camera (PI-MAX4, Princeton Instrument, USA) with a spectrometer (Acton SP2150, Princeton Instrument, USA) as the detector. The samples were placed in a closed-cycle helium cryostat to provide temperatures in the range from 20 to 300 K.

The optical 4f–5d transition energies of Ce<sup>3+</sup> in SAOH and SAOF were predicted by constrained density functional theory (cDFT) calculations with a plane-wave cutoff energy of 500 eV as the wave function.<sup>35,36</sup> The 2 × 2 × 2 supercells (Sr<sub>23</sub>Ce<sub>1</sub>Al<sub>8</sub>O<sub>33</sub>H<sub>7</sub>) were derived from the calculated primitive cell of SAOH containing 72 atoms with one Ce atom substituted on a Sr1 site and a Sr2 site. The DFT+*U* method was used for localizing the Ce *f* electrons inside the

band gap with a  $U$  value of  $U_{\text{eff}} = 5$  eV for both the hydride and fluoride materials.

The transition energies were calculated based on the configuration coordinated diagram (Figure S1). The excitation and emission processes were simulated as four electronic states: the ground state  $A_0$ , the excited state without structural relaxation  $A_0^*$ , the excited state after relaxation  $A^*$ , and the ground state with the relaxed structure  $A$ . When one electron of Ce in the 4f ground state is excited to the 5d level by absorbing photon energy, the excitation process occurs, which is represented by the  $A_0$  state to the  $A_0^*$  state. The disequilibrium of the electronic configuration in  $\text{Ce}^{3+}$  further leads to lattice relaxation in the excited state. The excited electron in the 5d level then returns to the 4f ground state by emission of a photon. This emission process is represented by the  $A^*$  state to the  $A$  state. The transition energies and Stokes shifts can be determined by the following equations:

$$E_{\text{abs}} = E_0^* - E_0$$

$$E_{\text{em}} = E^* - E$$

$$\Delta S = E_{\text{abs}} - E_{\text{em}}$$

In this study, correction of the transition energies was employed to improve the systematical error by the cDFT method as follows:<sup>37,38</sup>

$$E_{\text{abs-correct}} = (E_{\text{abs}} - 0.142)/1.01$$

$$E_{\text{em-correct}} = (E_{\text{em}} + 0.066)/1.08$$

## RESULTS AND DISCUSSION

The TOF-NPD pattern and refined crystal structure of SAOD are shown in Figure 1a. The crystallographic parameters obtained based on Rietveld refinement of the NPD data are listed in Table 1. As expected for the small peaks originating from S12A7 ( $\text{Sr}_{12}\text{Al}_{14}\text{O}_{33}$ ) and SrO impurities [1.32(5) and 1.71(6) wt %, respectively], most of the diffraction peaks are assigned to the  $\text{Sr}_3\text{AlO}_4\text{F}$ -type structure with space group  $I4/$

$mcm$  (No. 140) with lattice parameters of  $a = 6.76859(9)$  Å,  $c = 11.18568(2)$  Å, and  $V = 512.450(3)$  Å<sup>3</sup> (details of the refinement are given in Tables S1–S4). Refinement of the XRD pattern of SAOH gave the same structure with similar lattice parameters of  $a = 6.7560(1)$  Å,  $c = 11.1567(3)$  Å, and  $V = 509.24(2)$  Å<sup>3</sup> (Figure S2 and Tables S5 and S6), which are close to those of SAOF [ $a = 6.7668(2)$  Å,  $c = 11.1527(1)$  Å, and  $V = 510.68(4)$  Å<sup>3</sup>]. Thus, we assumed that deuteride and hydride ions substituted for the fluoride ion sites to form the oxyhydride without causing a structural phase transition owing to the comparable ionic radii of  $\text{H}^-$  and  $\text{F}^-$ . To assist in structure determination, structural relaxation of the SAOF and SAOH systems was performed by DFT calculations. The optimized lattice parameters were very close to the experimental parameters in both cases ( $a = 6.8035$  Å,  $c = 11.2706$  Å, and  $V = 521.68$  Å<sup>3</sup> for SAOH and  $a = 6.8300$  Å,  $c = 11.2638$  Å, and  $V = 525.444$  Å<sup>3</sup> for SAOF). The interatomic distance of Sr–H in this work is close to the value of the reported typical metal hydrides, indicating the existence of H–Sr bonds in SAOH (Table S7). The occupancy of the D site in SAOD was refined to 0.999(8) using the NPD data, and the H stoichiometry in SAOH was determined to be  $\text{H}/\text{Sr}_3\text{AlO}_4 = 1.05$  by TDS measurement, which agree well with the expected chemical composition. Notably, the H desorption peak of SAOH (Figure S3) started at around 500 °C under vacuum, which is comparable with the high temperatures for the hydride and oxyhydride materials and suggests remarkable thermal stability in an inert environment.<sup>39,40</sup> In the IR absorption spectrum of  $\text{Sr}_3\text{AlO}_4\text{H}$ , a strong peak centered at  $\sim 1050$   $\text{cm}^{-1}$  was observed, which was not observed in  $\text{Sr}_3\text{AlO}_4\text{F}$  and was attributed to the Sr–H stretching mode (Figure S4). In both  $\text{Sr}_3\text{AlO}_4\text{H}$  and  $\text{Sr}_3\text{AlO}_4\text{F}$ , the broad absorption bands corresponding to the bending and stretching vibration modes of surface-adsorbed  $\text{H}_2\text{O}$  were observed in the ranges of 1400–1600 and 2500–3700  $\text{cm}^{-1}$ , with small sharp peaks due to OH groups at 3500, 3600, and 3665  $\text{cm}^{-1}$ . These results indicate that H in bulk  $\text{Sr}_3\text{AlO}_4\text{H}$  exists mainly as  $\text{H}^-$  ions, while the surface of  $\text{Sr}_3\text{AlO}_4\text{H}$  is immediately hydrated to form OH groups after exposure to air.

SAOH can be described as a layered structure stacked along the  $c$  axis in which the isolated  $\text{AlO}_4$  tetrahedra whose O atoms coordinate to the Sr1 atoms are separated by  $\text{Sr}_2\text{H}$  layers, as shown in Figure 1b. In this structure, the nonequivalent Sr atoms (Sr1 and Sr2) occupy the Wyckoff positions 4a and 8h with 10- and 8-coordinate numbers, whereas H, Al, and O occupy the 4c, 4b, and 16l positions, respectively. Sr1 is surrounded by eight O and two apical H sites, while Sr2 is surrounded by six O sites and two H sites. Each hydride ion is bonded to two axial Sr1 atoms and four equatorial Sr2 atoms to form corner-sharing  $\text{Sr}_6\text{H}$  octahedra. Compared with SAOF, SAOH presents significant contraction of the  $a$ -axis length (−0.39%) with small elongation of the  $c$ -axis length (0.006%), which is consistent with the experimental results (−0.16% and 0.003%, respectively). Contraction of the  $a$ -axis length is probably related to the decrease of the Al1–Sr1 distance, while distortion of the  $\text{Sr}_6\text{F}$  octahedra may account for the small elongation of the  $c$ -axis length. Using the bond lengths optimized by DFT calculations, the bond-valence-sum (BVS) values were calculated for SAOF and SAOH to compare the stabilities of the ions (Tables S8–S10). The BVS value of H in SAOH was calculated to be 1.2129, which is almost the same as the value of F in SAOF (1.2133), proving that hydride ions

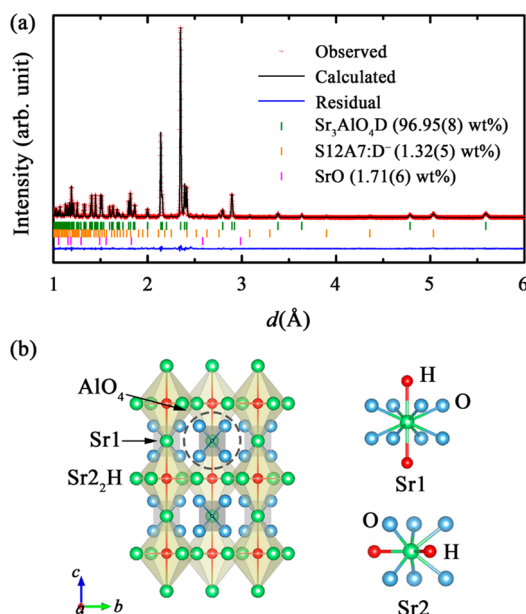


**Figure 1.** (a) TOF-NPD pattern of  $\text{Sr}_3\text{AlO}_4\text{D}$  (red crosses), Rietveld refinement (black line), and difference between the pattern and fitted pattern (blue line). The vertical bars below the pattern show the calculated positions of the Bragg diffractions for  $\text{Sr}_3\text{AlO}_4\text{D}$  (green), S12A7:D<sup>−</sup> (orange), and SrO (magenta). (b) Crystal structure of  $\text{Sr}_3\text{AlO}_4\text{H}$  and local coordination around Sr1 and Sr2.

**Table 1. Atomic Coordinates, Occupancies, and Isotropic Displacement Parameters of Sr<sub>3</sub>AlO<sub>4</sub>D Obtained by Rietveld Refinement Based on the NPD Pattern**

		occupancy	<i>x</i>	<i>y</i>	<i>z</i>	<i>U</i> <sub>iso</sub> (10 <sup>-2</sup> Å <sup>2</sup> )
Sr1	4a	1	0	0	1/4	0.964(2)
Sr2	8h	1	0.16887(19)	0.66887(19)	0	0.468(4)
Al1	4b	1	0	1/2	1/4	0.1460(2)
D1	4c	0.999(8)	0	0	0	1.934(3)
O1	16l	1	0.14204(15)	0.64204(15)	0.64829(13)	0.890(3)

can be stabilized in the fluoride ion sites to form the analogous oxyhydride.

Isovalent substitution of Ca<sup>2+</sup> and Ba<sup>2+</sup> for Sr<sup>2+</sup> in this oxyhydride system was also considered. In the previously reported Sr<sub>3-x</sub>A<sub>x</sub>AlO<sub>4</sub>F compounds, Ba<sup>2+</sup> prefers to occupy the 10-coordinated Sr1 sites, while Ca<sup>2+</sup> prefers to occupy the 8-coordinated Sr2 sites.<sup>41,42</sup> The same trend was observed for the Sr<sub>3-x</sub>A<sub>x</sub>AlO<sub>4</sub>H system by refinement of the XRD data and theoretical investigation through relaxed structure by DFT calculations. As shown by multiphase Rietveld refinement considering the small amount of impurity phases, Sr<sub>2</sub>CaAlO<sub>4</sub>H (SCAOH) also crystallized as the Sr<sub>3</sub>AlO<sub>4</sub>F-type structure with lattice parameters of *a* = 6.6219(2) Å, *c* = 10.9812(4) Å, and *V* = 481.53(3) Å<sup>3</sup> (Figure S5 and Table S11). To determine the Ca occupancy preference, three models were constructed for simulated XRD patterns from Rietveld refinements: Ca only occupying the Sr1 sites, Ca only occupying the Sr2 sites, and Ca occupying both the Sr1 and Sr2 sites. The refined occupancy of the mixing site of Sr and Ca well matched the intended composition and displayed a clear site preference of Ca for Sr2 sites (Table S12). Meanwhile, the major diffraction peaks of the Sr<sub>2</sub>BaAlO<sub>4</sub>H (SBAOH) sample were also well indexed to the Sr<sub>3</sub>AlO<sub>4</sub>F-type structure with lattice parameters of *a* = 6.90932(9) Å, *c* = 11.2106(2) Å, and *V* = 535.18(1) Å<sup>3</sup> (Figure S6 and Table S13). Partial substitution of Sr2 by Ca in SAOH led to a systematic decrease in the cell size, while replacement of Sr1 by Ba resulted in an increase in the cell size due to the difference in the cationic radii. Similar to Ca substitution in SCAOH, several models were constructed for Rietveld refinement, and Ba exhibited high site selectivity for the Sr1 site in SBAOH (Table S14). As mentioned above, the BVS values can be used to estimate the stability of atoms in local structures. In the SAOH host, the BVS value of Sr1 was calculated to be 1.309, which is less than its valence value (2+) and indicates its underbonded state. This underbonded structure allows possible substitution of the Sr1 site (*r* = 1.36 Å) by isovalent ions with larger ionic radii, such as Ba (*r* = 1.52 Å).<sup>43</sup> By incorporating Ba<sup>2+</sup> in the system, the BVS value of Ba/Sr1 increasing to 1.745 gives further proof. Conversely, the BVS value of the Sr2 site in SAOH was 2.107, indicating that cations with smaller ionic radii, such as Ca (*r* = 1.12 Å), are more suitable for introduction into the Sr2 site. In addition, we calculated the global instability indices (*G<sub>i</sub>*) based on the BVS values and compared the values among the SAOH, SCAOH, and SBAOH systems. The *G<sub>i</sub>* value measures the overall structural stability, and a structure with *G<sub>i</sub>* < 0.2 is considered to be empirically stable.<sup>44,45</sup> For the Sr<sub>3-x</sub>A<sub>x</sub>AlO<sub>4</sub>H (*A* = Ca, Ba; *x* = 0, 1) compounds, substitution of Ca or Ba into Sr sites contributes to the increasing structural stability because *G<sub>i</sub>* decreases from 0.217 for SAOH to 0.168 for SBAOH and 0.151 for SCAOH, respectively (Tables S16 and S18). This diminution of the *G<sub>i</sub>* value also demonstrates favorable substitution of Ba and Ca on the Sr sites. The

combination of experimental data and theoretical analysis reveals the preferential substitution of Ba on the Sr1 site and Ca on the Sr2 site in the Sr<sub>3-x</sub>A<sub>x</sub>AlO<sub>4</sub>H (*A* = Ca, Ba; *x* = 1) system. Moreover, the stability of the substituted structure may support the incorporation of various cations in this system. Despite the extreme air and moisture sensitivity of most hydride-based compounds, Sr<sub>3</sub>AlO<sub>4</sub>H was confirmed to be moderately reactive with moisture and decompose to Sr(OH)<sub>2</sub>·H<sub>2</sub>O and Sr<sub>3</sub>Al<sub>2</sub>O<sub>6</sub>·6H<sub>2</sub>O after exposure to ambient air (Figure S7). This reactivity can be further suppressed by partially substituting the Sr sites by Ca or Ba to form SCAOH or SBAOH. Decomposition of the SCAOH and SBAOH compounds was only observed after exposure to air for more than 7 and 10 days, respectively (Figures S8 and S9).

The DRS spectra of the Sr<sub>3-x</sub>A<sub>x</sub>AlO<sub>4</sub>H samples (*A* = Ca, Ba; *x* = 0, 1) were measured at room temperature in the wavelength range 200–1000 nm. The optical band-gap energies of SCAOH, SAOH, and SBAOH determined by Tauc plots (inset of Figure 2) with the Kubelka–Munk

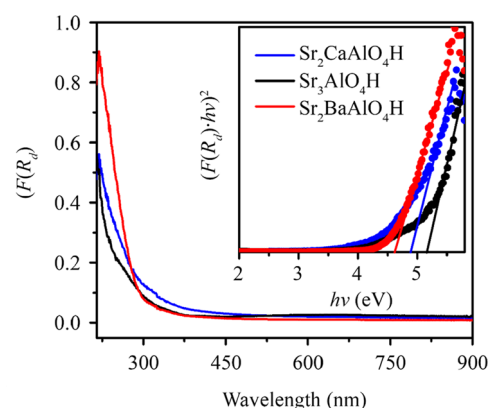


**Figure 2.** DRS spectra of Sr<sub>2</sub>CaAlO<sub>4</sub>H, Sr<sub>3</sub>AlO<sub>4</sub>H, and Sr<sub>2</sub>BaAlO<sub>4</sub>H. The inset shows the  $(F(R_d)hv)^2 - hv$  plots used to estimate the band-gap energies. The  $(F(R_d)hv)^2$  values for Sr<sub>2</sub>BaAlO<sub>4</sub>H were divided by 2 to set all of the data on the same coordinate axis.

function are 4.9, 5.1, and 4.6 eV, respectively.<sup>46</sup> First-principles calculations based on the PBE functional were performed to investigate the electronic structure of SAOH (Figure S10). In the PDOS, the conduction-band minimum is composed of Sr 4d orbitals and the valence-band maximum is derived from admixed O 2p and H 1s orbitals. SAOH is an insulator with a direct band gap of 4.535 eV. Meanwhile, the calculated band-gap values of SCAOH and SBAOH are 4.532 and 4.131 eV, respectively. Because of the limitations of the PBE functional, the calculated band-gap energies are normally underestimated. Therefore, the HSE06 functional was performed to obtain more realistic band-gap values. The HSE06 band gaps of SCAOH, SAOH, and SBAOH are 5.960, 5.997, and 5.596 eV, respectively (Table 2). The band-gap values estimated by the

**Table 2. Experimental Band-Gap Values of Sr<sub>2</sub>CaAlO<sub>4</sub>H, Sr<sub>3</sub>AlO<sub>4</sub>H, and Sr<sub>2</sub>BaAlO<sub>4</sub>H Compared with the Results Calculated with the PBE and HSE06 Functionals**

system	exptl (eV)	PBE (eV)	HSE06 (eV)
Sr <sub>2</sub> CaAlO <sub>4</sub> H	4.9	4.532	5.960
Sr <sub>3</sub> AlO <sub>4</sub> H	5.1	4.535	5.997
Sr <sub>2</sub> BaAlO <sub>4</sub> H	4.6	4.131	5.596

experimental spectra are 0.7–1.0 eV smaller than those predicted by the HSE06 calculations, revealing that the observed absorption edge originates from bulk excitons or defects (e.g., O<sup>2-</sup> and OH<sup>-</sup> in the H<sup>-</sup> site). Nevertheless, the series of Sr<sub>3-x</sub>A<sub>x</sub>AlO<sub>4</sub>H compounds can be identified as insulating materials and show white color in daylight. With a wide band gap required for phosphor hosts to suppress luminescence quenching, the Sr<sub>3-x</sub>A<sub>x</sub>AlO<sub>4</sub>H (A = Ca, Ba; x = 0, 1) compounds present show great potential for WLED applications. Because of the similarity of their ionic radii, optical activators, such as Ce and Eu, can be incorporated in the Sr sites, resulting in diverse luminescence properties.

Eu-doped Sr<sub>3-x-y</sub>A<sub>x</sub>Eu<sub>y</sub>AlO<sub>4</sub>H (A = Ca, Ba; x = 0, 1; y = 0.02) samples were prepared by partially substituting EuH<sub>2</sub> for SrH<sub>2</sub> in the starting materials and heating under a H<sub>2</sub> atmosphere. Eu<sup>2+</sup> is the most widely used activator in p-WLED applications because of its dipole-allowed 5d–4f transitions, and it provides various luminescence properties. Under excitation with near-UV light (365 nm), the Eu-doped oxyhydride samples emitted green luminescence. The emission and excitation spectra recorded at room temperature are displayed in Figure 3. All of the samples exhibited broad

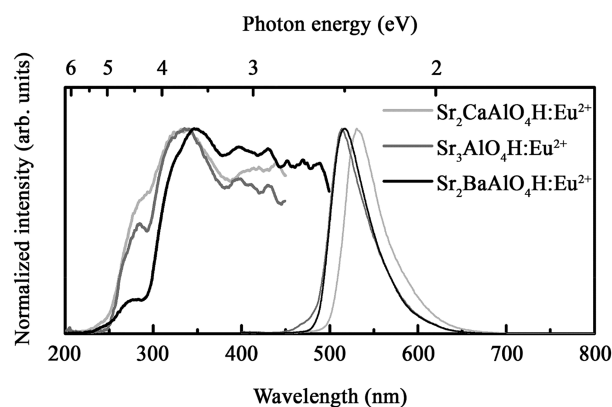


**Figure 3.** Emission and excitation spectra of Sr<sub>2</sub>CaAlO<sub>4</sub>H:Eu<sup>2+</sup> ( $\lambda_{em} = 530$  nm;  $\lambda_{ex} = 340$  nm), Sr<sub>3</sub>AlO<sub>4</sub>H:Eu<sup>2+</sup> ( $\lambda_{em} = 515$  nm;  $\lambda_{ex} = 340$  nm), and Sr<sub>2</sub>BaAlO<sub>4</sub>H:Eu<sup>2+</sup> ( $\lambda_{em} = 515$  nm;  $\lambda_{ex} = 350$  nm) measured at room temperature.

absorption bands from 250 to 450 nm with a maximum value at 340 nm (SCAOH:Eu<sup>2+</sup> and SAOH:Eu<sup>2+</sup>) or 350 nm (SBAOH:Eu<sup>2+</sup>), which can be assigned to the parity-allowed 4f<sup>7</sup> → 4f<sup>6</sup>5d<sup>1</sup> transitions of Eu<sup>2+</sup>. Under excitation with 350 nm light, all three samples showed narrow-band emission attributed to the transition between CFS 4f<sup>6</sup>5d<sup>1</sup> and ground-state 4f<sup>6</sup>. The emission bands of SAOH:Eu<sup>2+</sup> and SCAOH:Eu<sup>2+</sup> were centered at 515 nm with a full width at half-maximum (fwhm) of 51 nm, while that of SCAOH:Eu<sup>2+</sup> was centered at 530 nm with a fwhm of 50 nm. The number of Eu<sup>2+</sup> in SAOH was evaluated by the magnetization measurements fitted by the Brillouin function with  $J = 7/2$

corresponding to Eu<sup>2+</sup> with the <sup>8</sup>S<sub>7/2</sub> state. The well-fitted *M*–*H* curve gave the number of Eu<sup>2+</sup> corresponding to 95.3% of nominal Eu content, while the *M*–*T* curve gave the value of 89.9% (Figure S11). These results indicate that most of the Eu atoms form divalent states in SAOH:Eu. No additional emission peaks were observed, indicating complete reduction of Eu<sup>3+</sup> to Eu<sup>2+</sup> in this oxyhydride system. Note that in the analogous Eu-doped oxyfluoride compounds (i.e., Sr<sub>3-x</sub>A<sub>x</sub>AlO<sub>4</sub>F, where A = Ca, Ba), the Eu ions as activators only show the trivalent state even if prepared under a reduction atmosphere.<sup>41,47–49</sup> Thus, the present results demonstrate that the incorporation of hydride ligands in phosphor host materials can effectively stabilize Eu in the divalent state.

Ce-doped Sr<sub>3-x-y</sub>A<sub>x</sub>Ce<sub>y</sub>AlO<sub>4</sub>H (A = Ca, Ba; x = 0, 1; y = 0.02) samples were obtained by partially substituting CeH<sub>3</sub> for SrH<sub>2</sub> in the starting materials and heating under the same conditions. The phase purity was checked by the XRD pattern with Rietveld refinement. Under near-UV illumination (365 nm), all of the samples emitted green-yellow luminescence. The excitation and emission spectra of SAOH:Ce<sup>3+</sup> were collected with the respective maxima in the emission intensity, along with those of SCAOH:Ce<sup>3+</sup> and SBAOH:Ce<sup>3+</sup> (Figure 4). Each of these compounds exhibits a similar broad emission

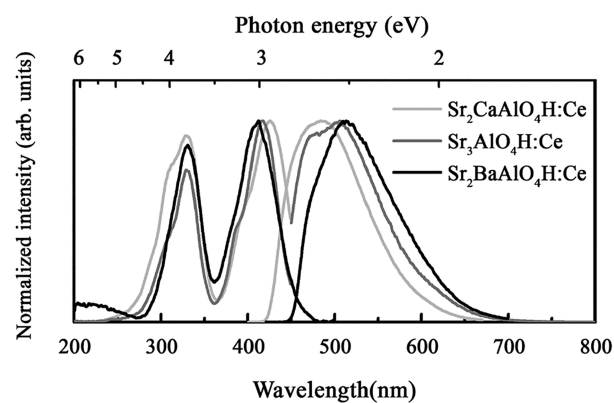


**Figure 4.** Emission and excitation spectra of Sr<sub>2</sub>CaAlO<sub>4</sub>H:Ce<sup>3+</sup> ( $\lambda_{em} = 500$  nm;  $\lambda_{ex} = 425$  nm), Sr<sub>3</sub>AlO<sub>4</sub>H:Ce<sup>3+</sup> ( $\lambda_{em} = 505$  nm;  $\lambda_{ex} = 415$  nm), and Sr<sub>2</sub>BaAlO<sub>4</sub>H:Ce<sup>3+</sup> ( $\lambda_{em} = 515$  nm;  $\lambda_{ex} = 410$  nm) measured at room temperature.

band in the range from 450 to 600 nm when excited by 425 and 410 nm light. When the substituent for the Sr site was changed from Ca to Ba, the emission spectrum presented a red shift, but the excitation spectrum showed a blue shift, which suggests that the Stokes shift increases in the following sequence: SCAOH:Ce<sup>3+</sup>, SAOH:Ce<sup>3+</sup>, and SBAOH:Ce<sup>3+</sup>. This can be further discussed in two aspects. The difference of the Stokes shift is probably correlated with the difference of the ionic radii. With the incorporation of larger cations, such as Ba<sup>2+</sup>, more significant distortion in the local structure can be achieved between the ground and excited states, which leads to large CFS of Ce 5d orbitals.<sup>42</sup> This difference of the Stokes shift can also be attributed to the opposite substitution preferences between Ca and Ba. Ba<sup>2+</sup> substitution occurs in the 10-coordinated Sr1 sites, while Ca<sup>2+</sup> substitution occurs in the 8-coordinated Sr2 sites. The broad emission peaks for both materials indicate the existence of two luminescence centers of Ce<sup>3+</sup>, which can be denoted as Ce1 and Ce2, corresponding to substitution on the Sr1 and Sr2 sites, respectively. In SBAOH, Ce<sup>3+</sup> ions prefer to occupy the Ce2 site because Ba<sup>2+</sup> with a

much larger ionic radius than  $\text{Ce}^{3+}$  ( $r = 1.12 \text{ \AA}$ ) exclusively occupies the Sr1 sites.<sup>43</sup> In contrast,  $\text{Ce}^{3+}$  ions prefer to occupy Ce1 sites in SCAOH. On the basis of the centroid shift model with the electronegativity values proposed by Pauling and corrected by Allred, the 8-coordinated Ce2 site is expected to have a stronger nephelauxetic effect and provide a larger centroid shift than the 10-coordinated Ce1 site.<sup>8,9,16</sup> Therefore, a larger Stokes shift is observed in SBAOH: $\text{Ce}^{3+}$  than in SCAOH: $\text{Ce}^{3+}$ . Additionally, the luminescence decay curves excited at 366 nm were measured for each sample at 20 K under vacuum. The decay curves of SCAOH: $\text{Ce}^{3+}$  and SBAOH: $\text{Ce}^{3+}$  of the emission of 530 nm can be well fitted by single-exponential functions with lifetimes of 37.3 and 29.9 ns, respectively (Figures S12 and S13).

To determine the hydride ligand effect on the luminescence properties, we compared the photoluminescence spectra of SAOH: $\text{Ce}^{3+}$  and SAOF: $\text{Ce}^{3+}$  (Figure 5). Under excitation by

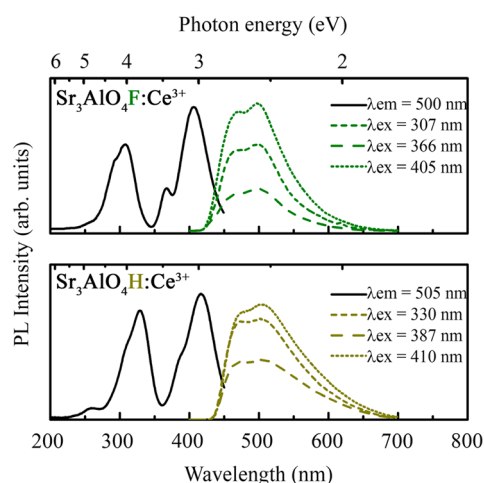


**Figure 5.** PLE and PL spectra of  $\text{Sr}_3\text{AlO}_4\text{F}:\text{Ce}^{3+}$  (top) and  $\text{Sr}_3\text{AlO}_4\text{H}:\text{Ce}^{3+}$  (bottom).

415 nm light, SAOH: $\text{Ce}^{3+}$  showed a broad emission band ranging from 450 to 700 nm, which corresponds to the transition of  $\text{Ce}^{3+}$  ions between the CFS  $4f^05d^1$  state and ground-state  $4f^1$  configuration. The asymmetric shape of the PL bands of SAOH: $\text{Ce}^{3+}$  can be well fitted into four Gaussian bands peaking at 467, 509, 568, and 634 nm, marked as I, II, III, and IV, respectively (Figure 6d). These doublet bands have energy differences of  $1790 \text{ cm}^{-1}$  between bands I and II and  $1840 \text{ cm}^{-1}$  between bands III and IV, indicating a spin-orbit splitting ( $\sim 1900 \text{ cm}^{-1}$ ) between the ground state ( $^2F_{7/2}$ ) and the lowest  $4f$  excited state of  $\text{Ce}^{3+}$  ( $^2F_{5/2}$ ).<sup>50</sup> This emission behavior suggests the existence of two different luminescence centers of  $\text{Ce}^{3+}$  ions in SAOH with different polyhedral geometries (Figure 1), which are denoted as Ce1 and Ce2. The decay curve of the 530 nm emission of SAOH: $\text{Ce}^{3+}$  can be fitted to a double-exponential function with a fast component of 31.8 ns and a slow component of 118.11 ns (Figure S14). In comparison, the emission band of SAOF: $\text{Ce}^{3+}$  was also deconvoluted into four Gaussian curves centered at 458, 497, 537, and 597 nm (Figure 6b). Therefore, we can clearly observe that each emission band of SAOH: $\text{Ce}^{3+}$  shifted to the longer-wavelength side compared with that of SAOF: $\text{Ce}^{3+}$ . The excitation spectra of SAOH: $\text{Ce}^{3+}$  monitored at 505 nm can be deconvoluted into four Gaussian components, consisting of two major bands centered at 333 and 417 nm (marked as b

and d) with two subordinate shoulder peaks at 317 and 383 nm (marked as a and c), which originate from CFS of the Ce 5d levels (Figure 6c). It should be noted that there was no significant difference in the positions and shapes of the emission bands for the three monitoring wavelengths of 330, 387, and 415 nm, which suggests that the major bands b and d possibly originated from one  $\text{Ce}^{3+}$  center, while the shoulder bands a and c originated from another  $\text{Ce}^{3+}$  center. As with SAOH: $\text{Ce}^{3+}$ , the excitation band of SAOF: $\text{Ce}^{3+}$  monitored at 500 nm can also be fitted by four Gaussian curves with two major bands at 313 and 406 nm (denoted as B and D) and two minor shoulders at 295 and 366 nm (denoted as A and C; Figure 6a). The positions of the deconvoluted PLE and PL peaks are listed in Table 3. The data show that the excitation bands of SAOH: $\text{Ce}^{3+}$  red-shifted (from 0.08 to 0.28 eV) compared with those of SAOF: $\text{Ce}^{3+}$ . The red shifts in both the excitation and emission bands in this oxyhydride compound compared with its isotopic oxyfluoride compound agree well with the reported hydride ligand effect in tuning of the optical properties and can be ascribed to large nephelauxetic effects.

To facilitate an understanding of the coordination geometry of  $\text{Ce}^{3+}$  in SAOH, cDFT calculations were performed to simulate the  $4f \rightarrow 5d$  transitions and compared with the experimental results. Charge compensation in the  $\text{Ce}^{3+}$  coordinated sites was achieved by replacing one neighboring  $\text{H}^-$  by  $\text{O}^{2-}$  ( $\text{O}_\text{H}$ ). The calculated transition energies and Stokes shifts of Ce1 and Ce2 in SAOH: $\text{Ce}^{3+}$  are given in Table 4. Note that cDFT calculations normally overestimate the transition energies for the  $\text{Ce}^{3+}$ -doped system, but they still provide reliable consistency with the experimental data.<sup>37</sup> The clear distinction between Ce1 and Ce2 can be seen by the larger excitation energy (4.15 eV) and smaller emission energy (2.25 eV) of Ce1, resulting in a large Stokes shift of 1.90 eV compared with that of Ce2 (0.33 eV). According to the cDFT results, excitation band d is assigned to the transition from 4f to the lowest 5d level of Ce1, while excitation band c is assigned to that of Ce2. Further, emission bands I and II are assigned to Ce2 (blue), and bands III and IV are assigned to Ce1 (green). Therefore, the Stokes shifts for Ce1 and Ce2 are estimated to be 1.27 and 0.54 eV, respectively. This gives a reasonable difference between the theoretical and experimental values of the Stokes shifts of Ce1 (0.61 eV) and Ce2 (0.21 eV). The energy-level schemes for Ce1 and Ce2 are depicted in Figure 6. The larger Stokes shift for Ce1 can be further explained by the relaxed structure configurations in the excited state provided by the cDFT calculations. During structure relaxation in the excited state, the site geometry of Ce1 drastically changed, mainly presenting as shrinkage of the Ce1–H bond length from 3.12 Å for the ground state to 2.73 Å for the excited state. Meanwhile, the Ce2–H bond lengths remained practically unchanged during relaxation in the excited state (2.58 Å) compared with the ground state (2.54 Å) (Tables S19 and S20). The difference in the length behavior of Ce1–H and Ce2–H in the excited state is related to their lengths in the ground state. As shown by the larger Sr1–H distance (2.82 Å) than that of Sr2–H (2.53 Å), two linear hydride ions are loosely bounded by center cation Sr1. When Ce is incorporated in the Sr1 site, the strong Ce1– $\text{O}_\text{H}$  bond forces its length to 2.36 Å, which is close to the sum of the ionic radii of  $\text{Ce}^{3+}$  ( $\sim 1.1 \text{ \AA}$ ) and  $\text{O}^{2-}$  ( $\sim 1.4 \text{ \AA}$ ), Ce1 shifts toward the  $\text{O}_\text{H}$  side, and the length of weak Ce1–H bond extends to 3.12 Å. On the other hand, the Sr2–H distance is close to the sum, and such a large shift cannot be induced for

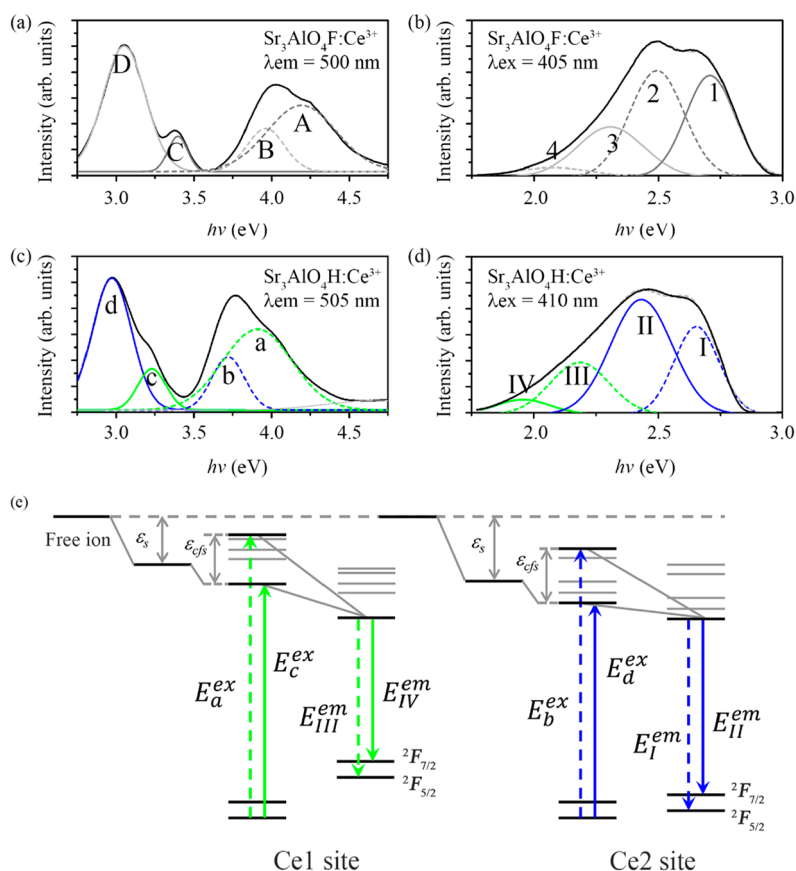


**Figure 6.** (a) Excitation and emission spectra of  $\text{Sr}_3\text{AlO}_4\text{F}:\text{Ce}^{3+}$ . The excitation band is fitted by four Gaussian curves marked as A–D. The emission band is divided into four Gaussian peaks marked as 1–4. (b–d) Excitation and emission spectra of  $\text{Sr}_3\text{AlO}_4\text{H}:\text{Ce}^{3+}$ . The excitation band is fitted by four Gaussian curves marked as a–d. The emission band is divided into four Gaussian peaks marked as I–IV. (e) Energy-level schemes of the Ce1 and Ce2 sites in  $\text{Sr}_3\text{AlO}_4\text{H}$  from the experimental and theoretical results.

**Table 3. Deconvoluted PLE and PL Peak Positions for  $\text{Sr}_3\text{AlO}_4\text{H}$  and  $\text{Sr}_3\text{AlO}_4\text{F}$**

	Deconvoluted PLE Peaks (eV)			
	A, a	B, b	C, c	D, d
$\text{Sr}_3\text{AlO}_4\text{F}:\text{Ce}^{3+}$	4.19	3.96	3.39	3.05
$\text{Sr}_3\text{AlO}_4\text{H}:\text{Ce}^{3+}$	3.91	3.72	3.23	2.97
	Deconvoluted PL Peaks (eV)			
	1, I	2, II	3, III	4, IV
$\text{Sr}_3\text{AlO}_4\text{F}:\text{Ce}^{3+}$	3.08	2.49	2.30	2.07
$\text{Sr}_3\text{AlO}_4\text{H}:\text{Ce}^{3+}$	2.65	2.43	2.18	1.96

Ce2. In the excited state, the Ce 5d electron occupies the antibonding state of the Ce1–O<sub>H</sub> bond and induces elongation of the bond. In contrast, there is no space to shift Ce2 toward the H<sup>−</sup> side. Therefore, we only observed the obvious change of the Ce1–H distance between the ground and excited states. On the basis of the Dorenbos model, a shortening of the bond length yields stronger CFS of the Ce 5d<sup>1</sup> configuration.<sup>26,51–54</sup> This greater distortion of the Ce1 coordinated structure during geometry optimization in the excited state results in a larger Stokes shift than that of Ce2, which can be observed as smaller emission energies for Ce1.

Besides the Ce<sup>3+</sup> coordination geometry, cDFT calculations can also be utilized to discuss the difference in the luminescence properties between SAOH and its fluoride analogue SAOF. Although a large Stokes shift of Ce1 due to the nature of the

**Table 4. Calculated Transition Energies and Stokes Shifts for Ce1 and Ce2 in SAOH and SAOF Compared with the Experimental Data**

	$\text{Sr}_3\text{AlO}_4\text{H}$		$\text{Sr}_3\text{AlO}_4\text{F}$	
	Ce1	Ce2	Ce1	Ce2
exptl	c	d	C	D
$E_{\text{abs}}$	3.23	2.97	3.39	3.05
$E_{\text{em}}$	1.96	2.43	2.49	2.07
Stoke shifts	1.27	0.54	0.90	0.98
calcd	$\text{Sr}_3\text{AlO}_4\text{H}$		$\text{Sr}_3\text{AlO}_4\text{F}$	
	Ce1	Ce2	Ce1	Ce2
$E_{\text{abs}}$	4.15	3.26	4.33	3.91
$E_{\text{em}}$	2.25	2.93	3.40	2.99
Stoke shifts	1.90	0.33	0.93	0.92

Ce–H bond is expected for SAOH: $\text{Ce}^{3+}$ , the observed emission peak only exhibits a small red shift compared with that of SAOF: $\text{Ce}^{3+}$ . Therefore, both samples emit similar greenish luminescence under near-UV illumination. To determine the reason for this contradiction, we also performed cDFT calculations of the Ce-doped SAOF system. The calculated transition energies and Stokes shifts are listed in Table 4. In contrast to SAOH, the calculated Stokes shifts for Ce1 and Ce2 in SAOF are almost identical, with values of 0.93

and 0.92 eV, respectively. From the photoluminescence spectrum, it can be considered that the excitation band of **C** is the lowest 5d band of Ce1 (gray), while **D** is the lowest 5d band of Ce2 (light gray), and the emission bands **1** and **2** correspond to Ce1, while bands **3** and **4** correspond to Ce2. Then, the experimental Stokes shifts are estimated to be 0.90 eV for Ce1 and 0.98 eV for Ce2. Combining the theoretical and experimental analyses, the contrary contributions of Ce1 and Ce2 to the emission bands between SAOH and SAOF can be concluded as the reason for their similar luminescence color.

As mentioned above, large distortion of the coordination polyhedron around Ce1 in SAOH due to the electronic excitation leads to the large Stokes shift. The distortion is characterized by shrinkage of the Ce1–H bond, in other words, the displacement of Ce1 toward the H site along the *c* axis. In contrast, for the excited state of Ce1 in SAOF, the distortion is characterized by the displacement of Ce1 toward  $O_F$  ( $O^{2-}$  replacing  $F^-$  to maintain the 3+ state of Ce). One possible factor of this opposite behavior is the anisotropic antibonding character of the Ce 5d state due to mixed-anion coordination. Generally, the Ce 5d orbital in the compound has antibonding character along the direction from Ce to the ligand, and its occupation tends to increase the bond length. In SAOF, the antibonding character along the Ce1–F bond seems stronger than that along the Ce– $O_F$  bond, and then the Ce1–F distance is increased by occupation of the 5d state. On the other hand, in SAOH, the antibonding character along the Ce1–H bond is weaker than that along the Ce1– $O_H$  bond due to the nephelauxetic effect of H, causing a shortening of the Ce1–H distance. Note that the decrease of the Ce–H distance can be a secondary change associated with the decrease in the Ce–Sr distance because the nephelauxetic effect also enhances the extent and overlap of Ce 5d and Sr 4d orbitals, forming a bonding state in the  $Sr_3CeH$  octahedron.

## CONCLUSION

In summary, we have successfully synthesized a series of novel aluminate oxyhydrides,  $Sr_{3-x}A_xAlO_4H$  ( $A = Ca, Ba; x = 0, 1$ ), through a solid-state reaction of oxides and metal hydrides at 900 °C under 0.99 MPa of  $H_2$ . The crystal structures are isostructural to  $Sr_3AlO_4F$ , with full occupation of hydride (**D**) ions in the F sites. Both XRD and BVS analyses reveal that Ba prefers to incorporate in the 10-coordinated Sr1 sites and Ca presents a site preference for the 8-coordinated Sr2 sites. This opposite site selectivity fits with the difference in the ionic radii of  $Ba^{2+}$  (1.52 Å) and  $Ca^{2+}$  (1.12 Å). Green-emitting  $Sr_{3-x-y}A_xEu_yAlO_4H$  ( $A = Ca, Ba; x = 0, 1, y = 0.02$ ) compounds were developed with a narrow emission band centered at 510–530 nm (fwhm  $\approx$  50 nm). In contrast to the analogue  $Sr_3AlO_4F$ , we observed photoluminescence from  $Eu^{2+}$  doped in these oxyhydride systems, which suggests that hydride ligands can be considered to be good stabilizers of the divalent state of Eu. The Ce-doped  $Sr_{3-x-y}A_xCe_yAlO_4H$  ( $A = Ca, Ba; x = 0, 1; y = 0.02$ ) phosphors yield green luminescence under illumination of near-UV light. Compared with the analogous oxyfluoride phosphors, peak shifting of both the excitation and emission bands to the longer-wavelength range can be observed, which is consistent with the reported hydride- and oxyhydride-based phosphors.<sup>18–22</sup> This red shift can be explained by the large nephelauxetic effect caused by the high covalency of the hydride ligands. From the ab initio calculations, two different  $Ce^{3+}$  luminescence centers in the

SAOH system observed in the luminescence spectrum are validated. The large Stokes shifts of Ce1 (1.27 eV (experimental) and 1.90 eV (calculated)) are ascribed to the large CFS of the Ce 5d levels induced by distortion of the coordinated structure in the excited state. In addition to recently discovered silicate, borate, and phosphate hydride,<sup>22,23,55,56</sup> the current findings expand the class of oxyhydride materials stabilized by  $TO_4$  tetrahedral groups ( $T = Si, P, B, Al, \dots$ ) and show their potential as phosphors for optical applications.

## ASSOCIATED CONTENT

### Supporting Information

The Supporting Information is available free of charge at <https://pubs.acs.org/doi/10.1021/acs.inorgchem.0c02356>.

Computational details, Rietveld analysis of the NPD pattern, Rietveld refinement based on XRD patterns, TDS measurements, FTIR measurements, BVS analysis, formation energy calculations, moisture sensitivity, electronic structure, magnetization measurements, luminescence decay measurements, and calculated local coordination structure (PDF)

### Accession Codes

CCDC 2022080–2022082 and 2027220 contain the supplementary crystallographic data for this paper. These data can be obtained free of charge via [www.ccdc.cam.ac.uk/data\\_request/cif](http://www.ccdc.cam.ac.uk/data_request/cif), or by emailing [data\\_request@ccdc.cam.ac.uk](mailto:data_request@ccdc.cam.ac.uk), or by contacting The Cambridge Crystallographic Data Centre, 12 Union Road, Cambridge CB2 1EZ, UK; fax: +44 1223 336033.

## AUTHOR INFORMATION

### Corresponding Author

Satoru Matsuishi – Materials Research Center for Element Strategy, Tokyo Institute of Technology, Yokohama 226-8503, Japan; [orcid.org/0000-0001-8905-0255](https://orcid.org/0000-0001-8905-0255); Email: [matsuishi@mces.titech.ac.jp](mailto:matsuishi@mces.titech.ac.jp)

### Authors

Tong Wu – Materials Research Center for Element Strategy, Tokyo Institute of Technology, Yokohama 226-8503, Japan; [orcid.org/0000-0002-2460-2423](https://orcid.org/0000-0002-2460-2423)

Kotaro Fujii – Department of Chemistry, School of Science, Tokyo Institute of Technology, Tokyo 152-8551, Japan; [orcid.org/0000-0003-3309-9118](https://orcid.org/0000-0003-3309-9118)

Taito Murakami – Department of Chemistry, School of Science, Tokyo Institute of Technology, Tokyo 152-8551, Japan

Masatomo Yashima – Department of Chemistry, School of Science, Tokyo Institute of Technology, Tokyo 152-8551, Japan; [orcid.org/0000-0001-5406-9183](https://orcid.org/0000-0001-5406-9183)

Complete contact information is available at:

<https://pubs.acs.org/doi/10.1021/acs.inorgchem.0c02356>

### Notes

The authors declare no competing financial interest.

## ACKNOWLEDGMENTS

This work was supported by MEXT Elements Strategy Initiative to Form Core Research Center (Grant JPMXP0112101001) and JSPS KAKENHI (Grants 16H06440 and 16H06441). The neutron experiments at the Materials and Life Science Experimental Facility of the J-PARC

were performed under a user program (Proposal Numbers 2019B0202 and 2019B0121).

## REFERENCES

- (1) Kageyama, H.; Hayashi, K.; Maeda, K.; Attfeld, J. P.; Hiroi, Z.; Rondinelli, J. M.; Poeppelmeier, K. R. Expanding Frontiers in Materials Chemistry and Physics with Multiple Anions. *Nat. Commun.* **2018**, *9* (1), 772.
- (2) Yajima, T.; Takeiri, F.; Aidzu, K.; Akamatsu, H.; Fujita, K.; Yoshimune, W.; Ohkura, M.; Lei, S.; Gopalan, V.; Tanaka, K.; Brown, C. M.; Green, M. A.; Yamamoto, T.; Kobayashi, Y.; Kageyama, H. A Labile Hydride Strategy for the Synthesis of Heavily Nitridized BaTiO<sub>3</sub>. *Nat. Chem.* **2015**, *7* (12), 1017–1023.
- (3) Scaife, D. E. Oxide Semiconductors in Photoelectrochemical Conversion of Solar Energy. *Sol. Energy* **1980**, *25* (1), 41–54.
- (4) Hitoki, G.; Takata, T.; Kondo, J. N.; Hara, M.; Kobayashi, H.; Domen, K. An Oxynitride, TaON, as an Efficient Water Oxidation Photocatalyst under Visible Light Irradiation ( $\lambda \leq 500$  nm). *Chem. Commun.* **2002**, *2* (16), 1698–1699.
- (5) Zhao, L. D.; Berardan, D.; Pei, Y. L.; Byl, C.; Pinsard-Gaudart, L.; Drago, N. Bi<sub>1-x</sub>Sr<sub>x</sub>CuSeO Oxyselenides as Promising Thermoelectric Materials. *Appl. Phys. Lett.* **2010**, *97* (9), 092118.
- (6) Fornari, M.; Subedi, A.; Singh, D. J. Structure and Dynamics of Perovskite Hydrides AMgH<sub>3</sub> (A=Na, K, Rb) in Relation to the Corresponding Fluorides: A First-Principles Study. *Phys. Rev. B: Condens. Matter Mater. Phys.* **2007**, *76* (21), 214118.
- (7) Tortoza, M. S.; Humphries, T. D.; Sheppard, D. A.; Paskevicius, M.; Rowles, M. R.; Sofianos, M. V.; Aguey-Zinsou, K. F.; Buckley, C. E. Thermodynamics and Performance of the Mg-H-F System for Thermochemical Energy Storage Applications. *Phys. Chem. Chem. Phys.* **2018**, *20* (4), 2274–2283.
- (8) Pauling, L. The Theoretical Prediction of the Physical Properties of Many Electron Atoms and Ions. Mole Refraction, Diamagnetic Susceptibility, and Extension in Space. *Proc. R. Soc. London. Ser. A, Contain. Pap. a Math. Phys. Character* **1927**, *114* (767), 181–211.
- (9) Allred, A. L. Electronegativity Values from Thermochemical Data. *J. Inorg. Nucl. Chem.* **1961**, *17* (3–4), 215–221.
- (10) George, N. C.; Denault, K. A.; Seshadri, R. Phosphors for Solid-State White Lighting. *Annu. Rev. Mater. Res.* **2013**, *43* (1), 481–501.
- (11) Shao, B.; Huo, J.; You, H. Prevailing Strategies to Tune Emission Color of Lanthanide-Activated Phosphors for WLED Applications. *Adv. Opt. Mater.* **2019**, *7* (13), 1900319.
- (12) Clabau, F.; Rocquefelte, X.; Jobic, S.; Deniard, P.; Whangbo, M.-H.; Garcia, A.; Le Mercier, T. Mechanism of Phosphorescence Appropriate for the Long-Lasting Phosphors Eu<sup>2+</sup>-Doped SrAl<sub>2</sub>O<sub>4</sub> with Codopants Dy<sup>3+</sup> and B<sup>3+</sup>. *Chem. Mater.* **2005**, *17* (15), 3904–3912.
- (13) Hoerder, G. J.; Seibald, M.; Baumann, D.; Schröder, T.; Peschke, S.; Schmid, P. C.; Tyborski, T.; Pust, P.; Stoll, I.; Bergler, M.; Patzig, C.; Reißaus, S.; Krause, M.; Berthold, L.; Höche, T.; Johrendt, D.; Huppertz, H. Sr[Li<sub>2</sub>Al<sub>2</sub>O<sub>2</sub>N<sub>2</sub>]:Eu<sup>2+</sup>—A High Performance Red Phosphor to Brighten the Future. *Nat. Commun.* **2019**, *10* (1), 1824.
- (14) Pust, P.; Weiler, V.; Hecht, C.; Tücks, A.; Wochnik, A. S.; Henß, A. K.; Wiechert, D.; Scheu, C.; Schmidt, P. J.; Schnick, W. Narrow-Band Red-Emitting Sr[LiAl<sub>3</sub>N<sub>4</sub>]:Eu<sup>2+</sup> as a next-Generation LED-Phosphor Material. *Nat. Mater.* **2014**, *13* (9), 891–896.
- (15) Dorenbos, P. Energy of the First 4f<sup>7</sup>→4f<sup>6</sup>5d Transition of Eu<sup>2+</sup> in Inorganic Compounds. *J. Lumin.* **2003**, *104* (4), 239–260.
- (16) Dorenbos, P. Ce<sup>3+</sup> 5d-Centroid Shift and Vacuum Referred 4f-Electron Binding Energies of All Lanthanide Impurities in 150 Different Compounds. *J. Lumin.* **2013**, *135*, 93–104.
- (17) Meijerink, A.; Dirksen, G. J. Spectroscopy of Divalent Samarium in LiBaF<sub>3</sub>. *J. Lumin.* **1995**, *63* (4), 189–201.
- (18) Kunkel, N.; Kohlmann, H.; Sayede, A.; Springborg, M. Alkaline-Earth Metal Hydrides as Novel Host Lattices for Eu<sup>II</sup> Luminescence. *Inorg. Chem.* **2011**, *50* (13), 5873–5875.
- (19) Kunkel, N.; Meijerink, A.; Kohlmann, H. Bright Yellow and Green Eu(II) Luminescence and Vibrionic Fine Structures in LiSrH<sub>3</sub>, LiBaH<sub>3</sub>, and Their Corresponding Deuterides. *Phys. Chem. Chem. Phys.* **2014**, *16* (10), 4807–4813.
- (20) Kunkel, N.; Meijerink, A.; Kohlmann, H. Variation of the Eu<sup>II</sup> Emission Wavelength by Substitution of Fluoride by Hydride in Fluorite-Type Compounds EuH<sub>x</sub>F<sub>2-x</sub> (0.20 ≤ x ≤ 0.67). *Inorg. Chem.* **2014**, *53* (10), 4800–4802.
- (21) Ueda, J.; Matsui, S.; Tokunaga, T.; Tanabe, S. Preparation, Electronic Structure of Gadolinium Oxyhydride and Low-Energy 5d Excitation Band for Green Luminescence of Doped Tb<sup>3+</sup> Ions. *J. Mater. Chem. C* **2018**, *6* (28), 7541–7548.
- (22) Gehlhaar, F.; Finger, R.; Zapp, N.; Bertmer, M.; Kohlmann, H. LiSr<sub>2</sub>SiO<sub>4</sub>H, an Air-Stable Hydride as Host for Eu(II) Luminescence. *Inorg. Chem.* **2018**, *57* (19), 11851–11854.
- (23) Wu, T.; Ishikawa, A.; Honda, T.; Tamatsukuri, H.; Ikeda, K.; Otomo, T.; Matsui, S. Nephelauxetic Effect of the Hydride Ligand in Sr<sub>2</sub>LiSiO<sub>4</sub>H as a Host Material for Rare-Earth-Activated Phosphors. *RSC Adv.* **2019**, *9* (10), 5282–5287.
- (24) Huang, B.; Corbett, J. D. Ba<sub>3</sub>AlO<sub>4</sub>H: Synthesis and Structure of a New Hydrogen-Stabilized Phase. *J. Solid State Chem.* **1998**, *141* (2), 570–575.
- (25) Zumdick, M.; Althoff, G.; Röhr, C. Barium Oxoaluminate Hydride. *Acta Crystallogr., Sect. C: Cryst. Struct. Commun.* **2001**, *C57* (4), 339–340.
- (26) Li, G.; Tian, Y.; Zhao, Y.; Lin, J. Recent Progress in Luminescence Tuning of Ce<sup>3+</sup> and Eu<sup>2+</sup>-Activated Phosphors for PC-WLEDs. *Chem. Soc. Rev.* **2015**, *44* (23), 8688–8713.
- (27) Shang, M.; Li, C.; Lin, J. How to Produce White Light in a Single-Phase Host? *Chem. Soc. Rev.* **2014**, *43* (5), 1372–1386.
- (28) Dorenbos, P. Relation between Eu<sup>2+</sup> and Ce<sup>3+</sup> f ↔ d-Transition Energies in Inorganic Compounds. *J. Phys.: Condens. Matter* **2003**, *15* (27), 4797–4807.
- (29) Hoshina, T. 5d→4f Radiative Transition Probabilities of Ce<sup>3+</sup> and Eu<sup>2+</sup> in Crystals. *J. Phys. Soc. Jpn.* **1980**, *48* (4), 1261–1268.
- (30) Coelho, A. A. TOPAS and TOPAS-Academic: An Optimization Program Integrating Computer Algebra and Crystallographic Objects Written in C++. *J. Appl. Crystallogr.* **2018**, *51* (1), 210–218.
- (31) Blöchl, P. E. Projector Augmented-Wave Method. *Phys. Rev. B: Condens. Matter Mater. Phys.* **1994**, *50* (24), 17953–17979.
- (32) Kresse, G. From Ultrasoft Pseudopotentials to the Projector Augmented-Wave Method. *Phys. Rev. B: Condens. Matter Mater. Phys.* **1999**, *59* (3), 1758–1775.
- (33) Perdew, J. P.; Burke, K.; Ernzerhof, M. Generalized Gradient Approximation Made Simple. *Phys. Rev. Lett.* **1996**, *77* (18), 3865–3868.
- (34) Oishi, R.; Yonemura, M.; Nishimaki, Y.; Torii, S.; Hoshikawa, A.; Ishigaki, T.; Morishima, T.; Mori, K.; Kamiyama, T. Rietveld Analysis Software for J-PARC. *Nucl. Instrum. Methods Phys. Res., Sect. A* **2009**, *600* (1), 94–96.
- (35) Degoli, E.; Guerra, R.; Iori, F.; Magri, R.; Marri, I.; Pulci, O.; Bisi, O.; Ossicini, S. Ab-Initio Calculations of Luminescence and Optical Gain Properties in Silicon Nanostructures. *C. R. Phys.* **2009**, *10* (6), 575–586.
- (36) Jia, Y.; Miglio, A.; Poncé, S.; Gonze, X.; Mikami, M. First-Principles Study of Ce<sup>3+</sup>-Doped Lanthanum Silicate Nitride Phosphors: Neutral Excitation, Stokes Shift, and Luminescent Center Identification. *Phys. Rev. B: Condens. Matter Mater. Phys.* **2016**, *93* (15), 155111.
- (37) Jia, Y.; Poncé, S.; Miglio, A.; Mikami, M.; Gonze, X. Assessment of First-Principles and Semiempirical Methodologies for Absorption and Emission Energies of Ce<sup>3+</sup>-Doped Luminescent Materials. *Adv. Opt. Mater.* **2017**, *5* (7), 1600997.
- (38) Jia, Y.; Miglio, A.; Mikami, M.; Gonze, X. Ab Initio Study of Luminescence in Ce-Doped Lu<sub>2</sub>SiO<sub>5</sub>: The Role of Oxygen Vacancies on Emission Color and Thermal Quenching Behavior. *Phys. Rev. Mater.* **2018**, *2* (12), 125202.
- (39) Fjellvåg, Ø. S.; Armstrong, J.; Sławiński, W. A.; Sjøstad, A. O. Thermal and Structural Aspects of the Hydride-Conducting Oxyhydride La<sub>2</sub>LiHO<sub>3</sub> Obtained via a Halide Flux Method. *Inorg. Chem.* **2017**, *56* (18), 11123–11128.

- (40) Paskevicius, M.; Sheppard, D. A.; Williamson, K.; Buckley, C. E. Metal Hydride Thermal Heat Storage Prototype for Concentrating Solar Thermal Power. *Energy* **2015**, *88*, 469–477.
- (41) Park, S.; Vogt, T. Near UV Excited Line and Broad Band Photoluminescence of an Anion-Ordered Oxyfluoride. *J. Am. Chem. Soc.* **2010**, *132* (13), 4516–4517.
- (42) Park, S.; Vogt, T. Defect Monitoring and Substitutions in  $\text{Sr}_{3-x}\text{A}_x\text{AlO}_4\text{F}$  (A = Ca, Ba) Oxyfluoride Host Lattices and Phosphors. *J. Phys. Chem. C* **2010**, *114* (26), 11576–11583.
- (43) Shannon, R. D. Revised Effective Ionic Radii and Systematic Studies of Interatomic Distances in Halides and Chalcogenides. *Acta Crystallogr., Sect. A: Cryst. Phys., Diffraction, Theor. Gen. Crystallogr.* **1976**, *32* (5), 751–767.
- (44) Brown, I. D. Recent Developments in the Methods and Applications of the Bond Valence Model. *Chem. Rev.* **2009**, *109* (12), 6858–6919.
- (45) Quilty, C. D.; Avdeev, M.; Driskell, J. D.; Sullivan, E. Structural Characterization and Photoluminescence in the Rare Earth-Free Oxy-Fluoride Anti-Perovskites  $\text{Sr}_{3-x}\text{Bi}_{2x/3}\text{AlO}_4\text{F}$  and  $\text{Sr}_{3-x}\text{Bi}_{2x/3}\text{GaO}_4\text{F}$ . *Dalton Trans.* **2017**, *46* (12), 4055–4065.
- (46) Kubelka, P.; Munk, F. The Kubelka-Munk Theory of Reflectance. *Zeit. Für. Tekn. Phys.* **1931**, *12*, 593–599.
- (47) Bandi, V. R.; Grandhe, B. K.; Woo, H.; Jang, K.; Shin, D.; Yi, S.-S.; Jeong, J.-H. Luminescence and Energy Transfer of  $\text{Eu}^{3+}$  or/and  $\text{Dy}^{3+}$  Co-Doped in  $\text{Sr}_3\text{AlO}_4\text{F}$  Phosphors with NUV Excitation for WLEDs. *J. Alloys Compd.* **2012**, *538*, 85–90.
- (48) Shang, M.; Li, G.; Kang, X.; Yang, D.; Geng, D.; Lin, J. Tunable Luminescence and Energy Transfer Properties of  $\text{Sr}_3\text{AlO}_4\text{F}:\text{RE}^{3+}$  (RE = Tm/Tb, Eu, Ce) Phosphors. *ACS Appl. Mater. Interfaces* **2011**, *3* (7), 2738–2746.
- (49) Fang, Y.; Li, Y. Q.; Qiu, T.; Delsing, A. C. A.; de With, G.; Hintzen, H. T. Photoluminescence Properties and Local Electronic Structures of Rare Earth-Activated  $\text{Sr}_3\text{AlO}_4\text{F}$ . *J. Alloys Compd.* **2010**, *496* (1–2), 614–619.
- (50) Blasse, G.; Grabmaier, B. C. Rare Earth Ions (Line Emission). *Luminescent Materials* **1994**, p40–49.
- (51) Dorenbos, P. Crystal Field Splitting of Lanthanide  $4f^{n-1}5d$ -Levels in Inorganic Compounds. *J. Alloys Compd.* **2002**, *341* (1–2), 156–159.
- (52) Dorenbos, P.  $5d$ -Level Energies of  $\text{Ce}^{3+}$  and the Crystalline Environment. III. Oxides Containing Ionic Complexes. *Phys. Rev. B: Condens. Matter Mater. Phys.* **2001**, *64* (12), 125117.
- (53) Dorenbos, P.  $5d$ -Level Energies of  $\text{Ce}^{3+}$  and the Crystalline Environment. I. Fluoride Compounds. *Phys. Rev. B: Condens. Matter Mater. Phys.* **2000**, *62* (23), 15640–15649.
- (54) Kunkel, N.; Wylezich, T. Recent Advances in Rare Earth-Doped Hydrides. *Z. Anorg. Allg. Chem.* **2019**, *645* (3), 137–145.
- (55) Mutschke, A.; Wylezich, T.; Ritter, C.; Karttunen, A. J.; Kunkel, N. An Unprecedented Fully  $\text{H}^-$ -Substituted Phosphate Hydride  $\text{Sr}_5(\text{PO}_4)_3\text{H}$  Expanding the Apatite Family. *Eur. J. Inorg. Chem.* **2019**, *2019* (48), 5073–5076.
- (56) Wylezich, T.; Valois, R.; Suta, M.; Mutschke, A.; Ritter, C.; Meijerink, A.; Karttunen, A. J.; Kunkel, N. Borate Hydrides as a New Material Class: Structure, Computational Studies, and Spectroscopic Investigations on  $\text{Sr}_5(\text{BO}_3)_3\text{H}$  and  $\text{Sr}_5(^{11}\text{B}\text{O}_3)_3\text{D}$ . *Chem. Eur. J.* **2020**, *5*, 202002273.